Particle Image Correlation Spectroscopy (PICS): Retrieving Nanometer-Scale Correlations from High-Density Single-Molecule Position Data

S. Semrau and T. Schmidt

Physics of Life Processes, Leiden Institute of Physics, Leiden University, Leiden, The Netherlands

ABSTRACT   A new data analysis tool that resolves correlations on the nanometer length and millisecond timescale is derived. This tool, adapted from methods of spatiotemporal image correlation spectroscopy, exploits the high positional accuracy of single-particle tracking. While conventional tracking methods break down if multiple particle trajectories intersect, our method works in principle for arbitrarily large molecule densities and diffusion coefficients as long as individual molecules can be identified. The method is computationally cheap and robust and requires no a priori knowledge about the dynamical coefficients, as opposed to other methods. We demonstrate the validity of the method by Monte Carlo simulations and by application to single-molecule tracking data of membrane-anchored proteins in live cells. The results faithfully reproduce those obtained by conventional tracking. Upon activation, a fraction of the small GTPase H-Ras is confined to domains of <200 nm diameter, which further substantiates the prediction that membrane organization is a determinant in cellular signaling.

INTRODUCTION

Single-particle tracking (SPT) and image correlation microscopy (ICM) have been proven powerful tools for the investigation of local inhomogeneities in biological systems (1–6). Driven by recent discussions on the refinement of the classical fluid-mosaic model of the plasma membrane organization (7), both tools were applied to elucidate the contribution of lipid organization and protein interactions to the spatial organization of signaling molecules both in vitro and in vivo. Several structures have been suggested to influence the dynamics of membrane proteins; among these are clathrin-coated pits, caveolae, lipid rafts, and the cytoskeleton. Lipid rafts, especially, have been heavily discussed as possible organizational platforms for molecules involved in cell signaling (8). Their existence and the actual order of lipids in the plasma membrane is, however, still debated (9–12). Recent studies have revealed that protein-protein interactions may play an important role in the spatial organization of signaling proteins (13,14).

Single-particle tracking is ideally suited to study the dynamics of membrane molecules, as this method is able to locate optical probes with a high positional accuracy down to a few nanometers. While gold nanoparticles and fluorescent quantum dots, being relatively large, allow for extremely long observation times (1,3,15,16), labeling of proteins with fluorophores such as, e.g., eGFP or Cy5, is more suitable for biological applications. Those fluorophores, however, suffer from photobleaching. Therefore, tracking of individual molecules results in comparatively short trajectories (typically 10 steps), which makes the retrieval of individual trajectory dynamical information exceedingly difficult. However,

given that the biological system is quite stable, the number of observations obtained under the same conditions can be large, to enable determination of dynamic properties of membranes in great detail (17).

For the implementation of SPT, some a priori knowledge about the expected molecular behavior is needed since algorithms have to cope with the probabilistic nature of the tracking problem (3,18). This is especially a drawback for data taken at higher concentrations, where molecular trajectories can be accidentally mixed. Image correlation microscopy (ICM) (5) and fluorescence correlation spectroscopy (2,3) do not need any such prior information. However, both are regular imaging techniques limited in resolution by diffraction and thus by a spatial resolution of 200–300 nm.

To overcome the drawbacks of both SPT and ICM we have developed a robust analysis method that combines both techniques. The method is self-contained on any ensemble of diffusion steps and therefore does not need individual traces to be assigned like in SPT. Consequently, it can deal with arbitrarily high molecule densities and diffusion constants as long as individual molecules can be identified. The starting point of this method is a correlation function, analogous to spatiotemporal image correlation spectroscopy (STICS) (19,20). A qualitative criterion for the general applicability is given. Further, theoretical boundaries for the achievable accuracy are discussed. Finally, the validity of the method is demonstrated by application to data created by Monte Carlo simulations and analysis of experimental data (17). The latter proves the existence of functional domains smaller than 200 nm in the plasma membrane of 3T3-A14 fibroblast cells.

THEORY

For clarity, we develop the method for the ideal situation, without, e.g., bleaching of molecules. In Appendix A, a

---

rigorous treatment of nonideal situations is given, which includes the effects of a limited field of view, finite positional accuracy, finite exposure time, bleaching, and blinking of molecules.

Algorithm

An image I obtained from SPT experiments is described as a sum of delta peaks representing the positions $\mathbf{r_i}$ of the molecules:

$$I(\mathbf{r}) = \sum_{i=1}^{m} \delta(\mathbf{r} - \mathbf{r}_i), \quad \mathbf{r} = (x, y). \tag{1}$$

Here m is the number of molecules in image I. The delta functions represent only the positions of the molecules, and therefore information about the intensity of the molecules is discarded in Eq. 1. The positions are retrieved from the raw image by fitting with the point-spread function of the microscope as detailed in Schmidt et al. (18). For any pair of images, I_a and I_b, which are separated in time by a time lag of Δt, a spatiotemporal correlation function is defined

$$C(\mathbf{d}, \Delta t) = \frac{\langle \iint_A d\mathbf{r}\, I_a(\mathbf{r}) I_b(\mathbf{r} + \mathbf{d}) \rangle_{\Delta t}}{\langle m_a \rangle}, \tag{2}$$

where $\langle \dots \rangle_{\Delta t}$ denotes the ensemble average over all pairs of images separated by a time-lag Δt, and A is the area of the field of view of the microscope. The two images are shifted by $\mathbf{d}$ with respect to each other and subsequently correlated, i.e., the spatial integral of their product is calculated. If $\mathbf{d}$ coincides with a movement during the time-lag Δt, the correlation will be high. The precise connection to the diffusion dynamics is given below. Note that $C(\mathbf{d}, \Delta t)$ is basically the correlation function used in STICS (19,20), where the denominator is given by the average number of molecules in image I_a only. This normalization was chosen since it leads directly to the cumulative probability distribution of diffusion steps; see Eq. 5.

In an isotropic medium, the cumulative correlation function only depends on a distance l and time-lag Δt. By definition of $\mathbf{d}(\rho, \phi) = (\rho \cos\phi, \rho \sin\phi)$ with polar coordinates ρ and ϕ,

$$\begin{aligned} C_{\mathrm{cum}}(l, \Delta t) &= \int_0^l d\rho\, \rho \int_0^{2\pi} d\phi\, C(\mathbf{d}(\rho, \phi), \Delta t) \\ &= \frac{\langle \iint_A d\mathbf{r}\, I_a(\mathbf{r}) m_b(\mathbf{r}, l) \rangle_{\Delta t}}{\langle m_a \rangle} \\ &= \frac{\langle \sum_{i=1}^{m_a} m_b(\mathbf{r}_{ai}, l) \rangle_{\Delta t}}{\langle m_a \rangle}, \end{aligned} \tag{3}$$

where $\mathbf{r}_{ai}$ is the position of molecule i in image I_a and $m_b(\mathbf{r}, l) = \int_0^l d\rho\, \rho \int_0^{2\pi} d\phi\, I_b(\mathbf{r} + \mathbf{d}(\rho, \phi))$. The expression $m_b(\mathbf{r}, l)$ is the number of molecules in image I_b that lie in a circle with radius l around $\mathbf{r}$.

The algorithm to obtain $C_{\mathrm{cum}}(l, \Delta t)$ from experimental data, derived directly from Eq. 3 and the definition of $m_b(\mathbf{r}, l)$,

is illustrated in Fig. 1: for each molecule position $\mathbf{r}_{ai}$ in image I_a, the number of molecules in image I_b are counted whose distance to $\mathbf{r}_{ai}$ is smaller or equal to l. Subsequently the contributions from all molecules in image I_a are summed and averaged over all image pairs. The division by the average number of molecules in image I_a finally results in $C_{\mathrm{cum}}(l, \Delta t)$.

Relation to diffusion dynamics

The expression $C_{\mathrm{cum}}(l, \Delta t)$ contains both temporal (i.e., diffusion of molecules) and spatial (i.e., random spatial proximity of molecules) correlations, which will be separated below. The spatial correlations are illustrated by the overlap of the circles in Fig. 1. Given that the molecules are identical, their movement is mutually uncorrelated, and the medium is homogeneous, $C_{\mathrm{cum}}(l, \Delta t)$ is simplified to

$$C_{\mathrm{cum}}(l, \Delta t) = \langle m_b(\tilde{\mathbf{r}}, l) \rangle_{\Delta t}, \tag{4}$$

where $\tilde{\mathbf{r}}$ is the arbitrary position of a molecule in image I_a. Note that the summation in Eq. 3 cancels out with the denominator $\langle m_a \rangle$ under the given assumptions. It should be mentioned that a global flow of the molecules is admissible. The same holds for interactions between molecules if they can be sufficiently described by a mean-field approximation. The part of Eq. 4 that is caused by accidental spatial proximity of different molecules is equal to the mean number of molecules in a circle with radius l around a certain fixed but arbitrary molecule. Given that the molecules are distributed uniformly and independently with a density c, the probability to find μ molecules in this circle is given by a Poisson distribution with mean and variance of: $\overline{\mu} = (\mu - \overline{\mu})^2 = c\pi l^2$, where c can be estimated as $c = (\langle m_b \rangle - 1)/A$. The latter
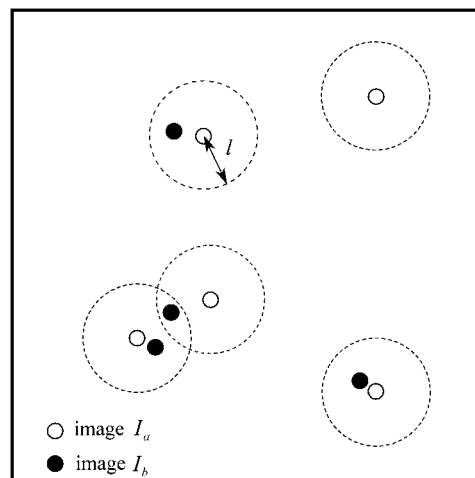
FIGURE 1 Particle image correlation spectroscopy (PICS) algorithm. For each molecule in image I_a (*open circles*) the number of molecules in image I_b (*solid circles*) closer than l is counted (five, in this example). Note that the peak in the center that lies within the overlap of two circles will be counted twice. Hence, the contribution that is due to diffusion is four, whereas one count is due to random spatial proximity of molecules.

assumption is justified, given that the ensemble average usually comprises many images of many different cells. Note that the precise definition of c is the density of the neighbors of a certain molecule. For higher densities this equals the total density, since then $(\langle m_b \rangle - 1)/A \approx \langle m_b \rangle/A$.

The part of Eq. 4 that contains the diffusion dynamics of the molecules is equal to the cumulative probability $P_{cum}(l, \Delta t)$ to find a diffusion step with a size smaller than l if the time lag is Δt. For normal diffusion with diffusion coefficient D in two dimensions,

$$P_{cum}(l, \Delta t) = 1 - \exp\left(-\frac{l^2}{4D\Delta t}\right).$$

The combination of both contributions leads to the following form of $C_{cum}(l, \Delta t)$:

$$C_{cum}(l, \Delta t) = P_{cum}(l, \Delta t) + c\pi l^2. \qquad (5)$$

The quantity calculated from experimental data by the algorithm described above (Eq. 3) is an estimator for this theoretically expected value. We now define a typical length-scale l_{cum} by

$$P_{cum}(l_{cum}, \Delta t) = 1/2. \qquad (6)$$

After subtraction of $c\pi l^2$ from C_{cum} this length scale can be determined and the diffusion constant is calculated as

$$D\Delta t = \frac{1}{\ln 2}\left(\frac{l_{cum}}{2}\right)^2. \qquad (7)$$

Figure of merit and achievable accuracy

Determination of $P_{cum}(l, \Delta t)$ from Eq. 5 is only practical if the variance of the second term $c\pi l^2$ is sufficiently small. Since the average of M statistically uncorrelated pairs of images is taken, the variance is $1/M$ times the value given above for the single Poisson process. Note that successive *pairs* of images are statistically uncorrelated since diffusion is a Markov process, whereas successive images are necessarily correlated. To get a qualitative criterion for the number of image pairs to be taken for a significant result, the standard deviation of the spatial correlations at l_{cum} (given by Eq. 7) is compared to the value of $P_{cum}(l, \Delta t)$ at l_{cum}:

$$\sqrt{\frac{c\pi l_{cum}^2}{M}} \ll \frac{1}{2}. \qquad (8)$$

We define a figure of merit η as twice this standard deviation

$$\eta = \sqrt{16\pi \ln 2 \frac{cD\Delta t}{M}}. \qquad (9)$$

Thus the result will be significant if $\eta \ll 1$. Note that molecules may be arbitrarily dense (provided that the over-

lapping images still allow them to be identified as individual molecules) or diffuse arbitrarily fast if only the number M of image-pairs is sufficiently large.

If the whole correction term is small, $c\pi l^2 \ll 1$, i.e.,

$$8\pi \ln 2c D\Delta t \ll 1, \qquad (10)$$

we directly obtain

$$C_{cum}(l, \Delta t) \approx P_{cum}(l, \Delta t). \qquad (11)$$

To get an error estimate for the diffusion constant D the probability density $P_{cum}(l, \Delta t)$ is shifted vertically by $\pm\eta/2$. From the calculation of the typical length scale l_{cum} of the shifted curves, boundaries for the values of D are retrieved,

$$\frac{1}{2} = P_{cum}(l_{cum}, \Delta t) \pm \frac{\eta}{2} \Rightarrow \frac{\Delta D}{\overline{D}} \approx \frac{\eta}{\ln 2}, \qquad (12)$$

for a sufficiently small η. $\overline{D}$ designates the mean D.

While this error originates from the method, there is an intrinsic spread of the values obtained for l_{cum} that is due to the stochastic nature of diffusion. If M pairs of images with $\langle m \rangle$ molecules on the average are acquired, the number of diffusion steps to be analyzed is $N = M\langle m \rangle$. The probability to find $N/2$ steps with a step-size smaller than l_{cum} is given by

$$f(l_{cum}; N) = KP_{cum}(l_{cum}, \Delta t)^{\frac{N}{2}}(1 - P_{cum}(l_{cum}, \Delta t))^{\frac{N}{2}}, \qquad (13)$$

where K is a normalization factor determined by $\int_0^\infty dl_{cum} f(l_{cum}; N) = 1$. This probability density for l_{cum} is depicted in Fig. 2 for various values of N. For an increasing number of diffusion steps, N, the function becomes symmetric about the value given by Eq. 7 and the width decreases. Hence the more images analyzed the less the spread in l_{cum}. Expansion of the exponentials in Eq. 13 around the maximum and estimation of the relative width for $N \gg 1$ yields $\Delta l_{cum}/\overline{l_{cum}} = (1/(2\ln 2))\sqrt{1 - (1/2)^{2/N}}$ where
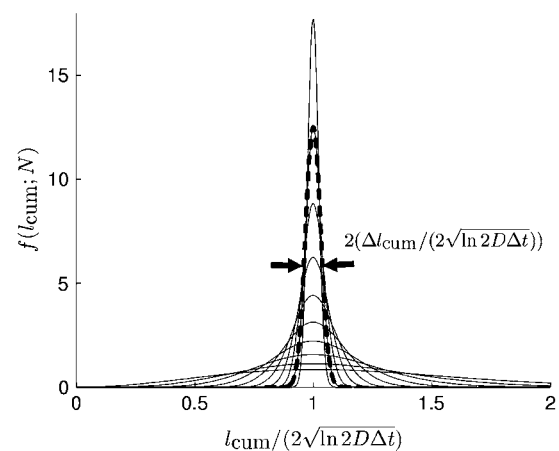
FIGURE 2 Probability density $f(l_{cum}; N)$ versus $l_{cum}/(2\sqrt{\ln 2D\Delta t})$ for $N = 2, 4, 8, \ldots, 1024$. The curve for $N = 1024$ corresponds to the sharpest distribution. For $N = 512$, expansion around the maximum was used to estimate the width of the distribution (*dashed curve*). Arrows indicate $2 \cdot (\Delta l_{cum}/(2\sqrt{\ln 2D\Delta t})$.

$\overline{l_{\text{cum}}}$ designates the mean l_{cum} and equals the value given by Eq. 7. Note that Δl_{cum} is defined analogous to the standard deviation as half the width of Eq. 13. Error propagation gives $\Delta D/\overline{D} = 2\Delta l/\overline{l_{\text{cum}}}$. To determine D with a relative error of ± 0.1, $N \approx 300$ diffusion steps are needed. Since the accuracy scales as $1/\sqrt{N}$ for $N \gg 1$, a relative error of ± 0.01 requires $N \approx 30,000$ steps. Note that this error estimation is only valid if the diffusion coefficient is determined from the typical length scale l_{cum} of $P_{\text{cum}}(l, \Delta t)$. For the scatter inherent to other analysis methods, see the article by Saxton (21).

Since the described errors are uncorrelated, the total error is

$$\frac{\Delta D_{\text{total}}}{\overline{D}} = \frac{1}{\ln 2}\sqrt{\eta^2 + (1 - (1/2)^{2/N})}. \tag{14}$$

For the adaptation of the method to nonideal situations that include, e.g., bleaching, see Appendix A.

Diffusion modes

Given that the criterion below Eq. 9 is fulfilled, the method developed up to this point is exact for the case of a single, normally diffusing species. For other (anomalous) cases (multiple fractions, intermittent, confined, or anisotropic diffusion, diffusion with trapping or, more generally, diffusion in a potential landscape), the diffusion coefficient determined as described above is only an estimation of the mean diffusion coefficient.

However, since the cumulative probability of step-sizes is intrinsic to the correlation function Eq. 5, analysis of data with more complicated diffusion models is straightforward. E.g., for a two-fraction case, which is important for the data analyzed below, molecules in image I_a are split in a fraction of size α with diffusion coefficient D_1 and one of size $1 - \alpha$ with diffusion coefficient D_2. This results in

$$P_{\text{cum}}(l, \Delta t) = \alpha\left(1 - \exp\left(-\frac{l^2}{r_1^2}\right)\right)$$
$$+ (1 - \alpha)\left(1 - \exp\left(-\frac{l^2}{r_2^2}\right)\right), \tag{15}$$

where $r_i^2 = 4D_i\Delta t, i \in \{1, 2\}$. Hence, the probability distribution $P_{\text{cum}}(l, \Delta t)$ can faithfully be used to analyze more complex inhomogeneous diffusion behavior.

MATERIALS AND METHODS

Monte Carlo simulations

For validation of the method, a Monte Carlo approach was used to generate random diffusion steps and determine the diffusion coefficient as described above. All simulations were performed within the MatLab programming environment (The MathWorks, Natick, MA). With the help of the standard MatLab routines for random number generation, M pairs of images were generated in the following way: the first image I_a consists of molecule

signals scattered uniformly over an area A_{sim}, which was bigger than the physical field of view of area A. This was necessary for the simulation of molecules that enter the area A during Δt. The value A_{sim} was taken large enough for the distribution of the molecules to be still approximately uniform in A after each time step Δt. The average number of molecules in A was fixed at five. Image I_b was obtained by letting each molecule in I_a perform a random step in x and y directions. The step-size in both spatial directions was determined by a Gaussian with variance $2D\Delta t$, i.e., all simulated molecules obeyed normal diffusion. Subsequently, all molecules that did not fall into the physical field of view were discarded. Furthermore, it was ensured that diffusion steps up to l_{max} were adequately represented as detailed in Appendix A. The algorithm derived above was subsequently executed for the values $l = \delta l, 2\delta l, \ldots, l_{\text{max}}$.

The value l_{cum} was found from $P_{\text{cum}}(l, \Delta t)$ by linear interpolation of the distribution at 0.5. The results were normalized to $2\sqrt{\ln 2D\Delta t}$ such that, according to Eq. 7, a value of 1 corresponds to the most probable l_{cum}. The whole simulation was repeated 1000 times and the results were divided into bins of width 0.05. The number of data points in each bin was subsequently divided by 1000, which resulted in relative frequencies for l_{cum}. For comparison of the simulation with theoretical predictions, the probability density derived in Eq. 13 was integrated over intervals of length 0.05, i.e., the bin size.

Since only a finite number of values for l can be considered, a binning error that depends on δl is introduced. Consequently, the distribution of the l_{cum} values will always deviate from Eq. 13. In Fig. 3, results for $\delta l = 0.01\sqrt{D\Delta t}$, $0.5\sqrt{D\Delta t}$, and $\sqrt{D\Delta t}$ are compared with $l_{\text{max}} = 3$. Since we choose a very small density and diffusion coefficient ($c = 2.5 \times 10^{-4}/\mu\text{m}^2$, $D\Delta t = 0.02~\mu\text{m}^2$), the deviation from the theoretical distribution Eq. 13 is caused by the binning error alone. Obviously the deviation decreases with decreasing δl. The simulations therefore use $\delta l = 0.01 \cdot \sqrt{D\Delta t}$. For smaller or bigger diffusion coefficients or time lags, l_{max} is scaled accordingly.

Single-molecule microscopy

The experiments were described in detail previously (17). In short, constitutive active human H-Ras (V12) and constitutive inactive human
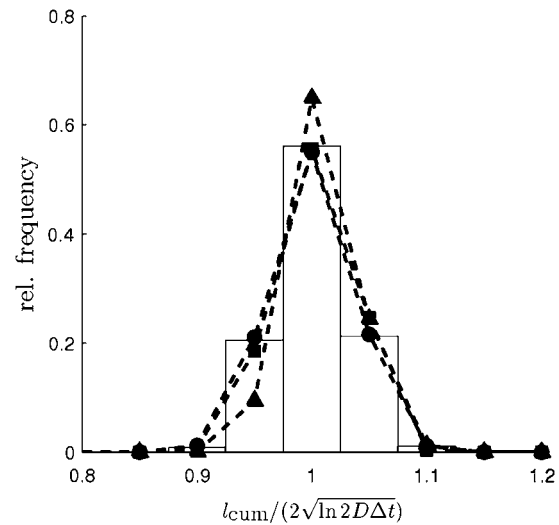
FIGURE 3 Binning error introduced into the estimation of l_{cum}. One-hundred image-pairs with diffusion constant $D = 1~\mu\text{m}^2/\text{s}$, $\Delta t = 20$ ms at a concentration of $c = 2.5 \times 10^{-4}/\mu\text{m}^2$ were used. The binning was set to triangle, $\delta l = \sqrt{D\Delta t}$; square, $\delta l = 0.5\sqrt{D\Delta t}$; and circle, $\delta l = 0.01\sqrt{D\Delta t}$, and compared to the distribution as given by Eq. 13 with $N = 500$ (bars).

H-Ras (N17) were coded into pcDNA3.1-eYFP (Qiagen, Hilden, Germany). Cells from a mouse fibroblast cell line stably expressing the human insulin receptor (3T3-A14) (22) were transfected with 1.0 μg DNA and 3 μl FuGENE 6 (Roche Molecular Biochemicals, Indianapolis, IN) per glass slide. 3T3-A14 cells adhered to glass slides were mounted onto the microscope and kept in PBS at 37°C. For the observation of the mobility of individual eYFP-H-Ras molecules, the focus of the microscope was set to the dorsal surface membrane of individual cells (depth of focus ≈ 1 μm). The density of fluorescent proteins on the plasma membrane of selected trans-fected cells was <1 μm^{-2} to permit imaging and tracking of individual fluo-rophores. Molecule positions were determined with an accuracy of ≈ 35 nm. Fluorescence images were taken consecutively with up to 1000 images per sequence. Typical trajectories were up to nine steps in length, mainly limited by the blinking and photobleaching of the fluorophore (23). Data sets were acquired with different time-lags Δt between consecutive images. The value Δt varied from 5 to 60 ms.

RESULTS

Monte Carlo simulations

The influence of a growing molecule density, c, and number of acquired image pairs M on the distribution were inves-tigated for fixed $D\Delta t$. The simulated concentrations corre-spond to a range of 0.1–10 molcules/μm^2 for typical experimental values ($D \approx 1$ μm^2/s, $\Delta t \approx 20$ ms).

The results for $M = 100$ and $M = 1000$ are presented in Fig. 4. For fixed M, the distribution of l_{cum} values broadens with rising molecule concentration. It should be noted that the distribution of l_{cum} always peaked around the true value. When the correction term for correlations due to random spatial proximity of molecules was omitted (i.e., the second term in Eq. 5), the peak l_{cum} values shifted to a lower value. Likewise the dependence of the method on the diffusion constant D and the number of image pairs M was studied for

a fixed molecule density. For typical experimental values ($c \approx 1/\mu$m^2, $\Delta t \approx 20$ ms), the diffusion constants correspond to a range from 0.1 μm^2/s to 10 μm^2/s. Results are shown in Fig. 4. The distribution broadens with D, similar to the results for growing molecule density. As predicted by Eq. 12, the distributions become narrower for growing M, which supports the claim that a higher number of image-pairs will compensate for a high molecular density or diffusion con-stant. The applicability of the method is, therefore, only limited by the number of images that can be acquired for identical conditions. The influence of bleaching and blinking on the distribution of l_{cum} is shown in Fig. 5. Molecules were assumed to turn dark with a probability p_{dark} per time-lag Δt. The distribution broadens if this probability is increased but stays peaked around the true value. The broadening is fully accounted for by the reduction of the statistical sample size $N = M\langle m \rangle$. E.g., for $p_{\text{dark}} = 0.9$, only 10% of molecules survive, leaving only 50 visible diffusion steps instead of 500 for $p_{\text{dark}} = 0$. We do not consider explicitly here that molecules can return into the fluorescent state (blinking), since the only effect is an increase in the apparent molecule density c, which was analyzed above.

Diffusional behavior of H-Ras mutants

Following the simulations, data on tracking individual H-Ras mutants on the plasma membrane of 3T3-A14 cells at 37°C, was analyzed. In a publication by Lommerse et al. (17), it was found that both the constitutive inactive (N17) as well the constitutive active (V12) variant of the protein displayed an inhomogeneous two-fraction diffusion behavior. In that ear-lier report the positions of proteins in an image sequence were used to calculate trajectories from which further information
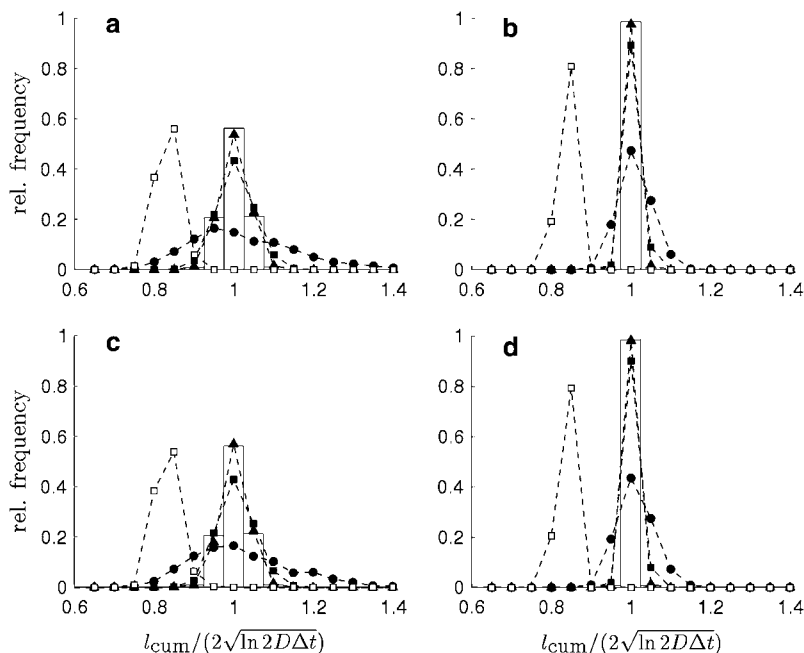
FIGURE 4 Distribution of l_{cum} from simulations. (*a,b*) Influence of molecule concentration at fixed $D\Delta t = 1$ μm^2/s and given number of images $M = 100$ (*a*), and $M = 1000$ (*b*) (*solid triangle*, $c = 0.1/\mu$m^2; *solid square*, $c = 1/\mu$m^2; *solid circle*, $c = 10/\mu$m^2; *open square*, same values as for the solid squares but without correction term; and *bars*, distribution as given by Eq. 13 with $N = 500$ for panel *a* and $N = 5000$ for panel *b*). (*c,d*) Influence of rising dif-fusion constant for constant $c = 1/\mu$m^2 and given number of images $M = 100$ (*c*), and $M = 1000$ (*d*). (*Solid triangle*, $D\Delta t = 0.1$ μm^2/s; *solid square*, $D\Delta t = 1$ μm^2/s; *solid circle*, $D\Delta t = 10$ μm^2/s; *open square*, same values as for the solid squares but without correction term; and *bars*, distribution as given by Eq. 13 with $N = 500$ for panel *c* and $N = 5000$ for panel *d*.)
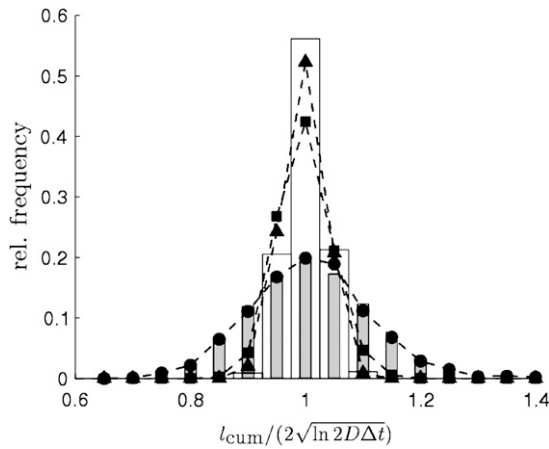
FIGURE 5 Distribution of l_{cum} from simulations including photobleaching. One-hundred image-pairs were analyzed at a concentration of $0.1/\mu m^2$, diffusion constant $D = 1 \ \mu m^2/s$, and time-lag $\Delta t = 20$ ms. (*Triangle*, $p_{dark} = 0$; *square*, $p_{dark} = 0.4$; *circles*, $p_{dark} = 0.9$; *open bars*, distribution as given by Eq. 13 with $N = 500$; and *shaded bars*, distribution as given by Eq. 13 with $N = 50$.)

on the mobility was extracted. Here the same position data is analyzed with the new algorithm without any a priori knowledge about molecular mobility.

The molecule density c was estimated from the experimental data. The slope of the linear part of $C_{cum}(l)$ when plotted versus l^2 (Fig. 6) directly equals $c \cdot \pi$. Note that c is by definition of this procedure exactly the density of neighboring molecules introduced above. Subtraction of the correction term $c\pi l^2$ successfully yielded $P_{cum}(l, \Delta t)$ for longer time lags (*solid data points* in Fig. 6). Artifacts due to diffraction observed for shorter time lags were removed
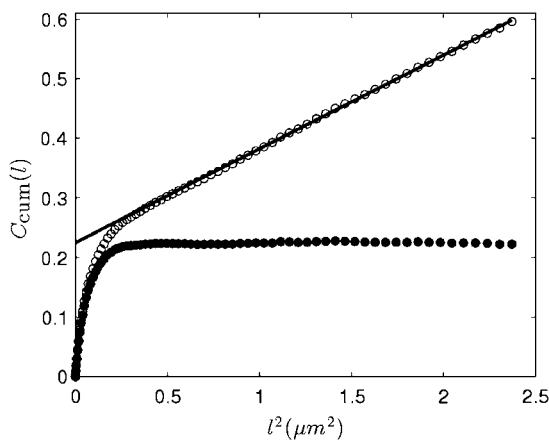
FIGURE 6 Experimentally obtained cumulative correlation function $C_{cum}(l)$. $C_{cum}(l)$ was obtained for individual H-Ras (N17) molecules at the apical side of 3T3-A14 cells with a time-lag Δt of 20 ms (*open circles*, $C_{cum}(l)$; *solid line*, linear fit of the long distance data yielded a concentration $c \approx 0.16/\mu m^2$; and *solid circle*, after subtraction of the correction term). Fit of the corrected data to Eq. 15 yielded $\alpha = 0.90 \pm 0.02$, $r_1^2 = 0.072 \pm 0.002 \ \mu m^2$, and $r_2^2 = 0.012 \pm 0.0003 \ \mu m^2$.

by an empirical, self-consistent algorithm, as detailed in Appendix B.

The value $P_{cum}(l, \Delta t)$ was subsequently constructed for each time-lag Δt between 4 and 60 ms. Data were fit according to the two-diffusing-fraction model (Eq. 15) to yield the fraction α and respective mean-square displacements r_1^2 and r_2^2 for both mutants.

Fig. 7 compares the results obtained by the new unbiased method (*solid symbols*, *solid lines*) with those obtained by conventional tracking methods (*open symbols*, *dashed lines*) in which an initial diffusion constant of $D = 1 \ \mu m^2/s$ had been assumed. Both data sets excellently match each other within experimental accuracy; see Table 1. For the inactive mutant (N17), 86% of the molecules fell into the highly mobile fraction characterized by a diffusion constant of $D_1 = 0.94 \ \mu m^2/s$. The slow fraction was characterized by a diffusion constant of $D_2 = 0.10 \ \mu m^2/s$. Both fractions followed free diffusion as seen by the linear dependence of the mean-square displacements (r_i^2) with Δt. In contrast, the slow diffusing fraction of the active mutant (V12) displayed a confined diffusion behavior (24) characterized by a confinement size of $L = 179$ nm. In addition, the diffusion constant of the fast, free diffusion fraction of the V12-mutant was reduced to $D_1 = 0.73 \ \mu m^2/s$ and the fraction size decreased to 63% in comparison to the inactive mutant N17.

DISCUSSION

The combination of the advantages of two well-established techniques, ICM and SPT, allowed the development of a robust analysis method, which retrieves spatiotemporal correlations on the sub-wavelength and millisecond timescale. By Monte Carlo simulations, the principle was proven, and it was shown that the method can deal with short traces, high molecule densities, and high diffusion constants provided that individual molecules can be identified and the total number of diffusion steps is sufficiently high. This holds even without an initial guess of the diffusion coefficients. Application to real experimental data shows that the method is simpler than conventional tracking while identical results are obtained. Structures with a diameter of <200 nm were faithfully identified. It should be noted, however, that the method is not applicable for nonergodic systems, i.e., if it becomes important that different molecules have different spatial environments. If the movement of the molecules is highly correlated, e.g., for interactions, which cannot be handled by a mean-field approach, correction schemes like the one presented in the Appendix have to be employed.

The results of change in mobility on the activation state of H-Ras by the new unbiased method further supports ideas of functional domains in the plasma membrane of mammalian cells. The results agree well with the results of the FRET (25), FRAP (26), EM (27), and single-molecule tracking experiments (17) in all of which functional domains have been observed. Likely localization of active H-Ras to these
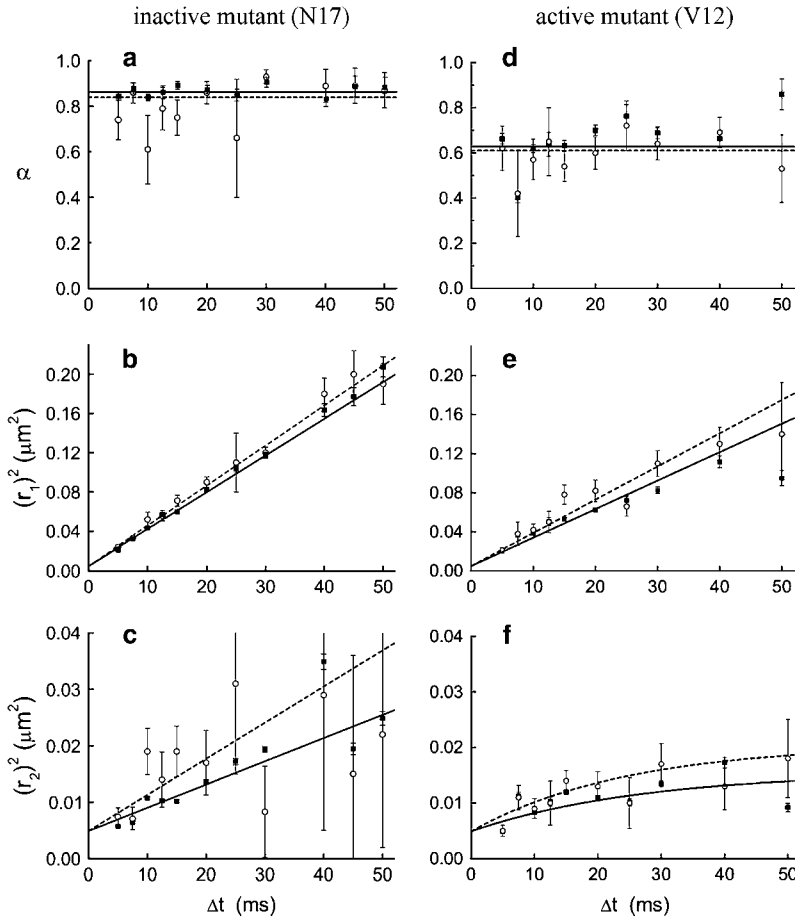
FIGURE 7 Diffusional behavior of H-Ras. Fraction α (a,d) and mean-square displacements r_1^2 (b,e) and r_2^2 (c,f) as functions of Δt for the constitutive inactive (N17) (a–c) and the constitutive active (V12) mutant (d–f) of H-Ras. (*Open circles, dashed lines* correspond to conventional tracking results (17); *solid squares, solid lines* to results obtained by the PICS method.) In the case of the conventional tracking, error bars correspond to the error of the fitting of the two-fraction model; for PICS, the size of the error bars is given by Eq. 14.

functional domains is not a static process, but is dynamic as suggested for trapping into cholesterol-independent domains (27) and into more general transient signaling complexes (25), which might be actin-dependent.

In summary, a robust method was presented that is superior to both ICM and SPT, surpassing the first in resolution and largely simplifying the analysis methods required for the second. Another intriguing application is the study of dynamical properties of interacting proteins in model membranes. Because the newly developed method allows the protein concentration to be varied over a wider range, a comparison to theoretical results obtained by a virial expansion is rendered possible.

APPENDIX A: BEYOND THE IDEAL SITUATION

Limited field of view

In the experimental situation, the field of view is always limited. Typically in the case of an epi-fluorescence setup the field of view is chosen in the center of the Gaussian beam profile so that the illumination can be considered uniform. Molecules, which diffuse out of view, not only limit the observation time but it is also more probable for a long step to end out of the field of view than for a small step. Consequently, long steps are underrepresented in the experimental distribution. Therefore, a reduced field of view is defined which has a width that is smaller than the full field of view by an amount of $2\,l_{max}$. Only those peaks of image I_a that lie within the reduced field of view are used. Thus, no steps are lost up to a length of l_{max}.

Finite positional accuracy

The limited positional accuracy makes a fixed molecule appear to move and a free molecule to diffuse faster. Since the real diffusive motion and the apparent motion due to the limited positional accuracy are uncorrelated, the fluctuations simply add so that

$$D_{meas}\Delta t = D_{real}\Delta t + \sigma^2, \qquad (16)$$

where D_{meas} is the measured diffusion coefficient, D_{real} is the real diffusion coefficient, and σ is the standard deviation of a Gaussian distribution that

TABLE 1 Comparison between results obtained by conventional tracking with results obtained by particle image correlation spectroscopy (PICS)

	Conventional tracking	PICS
H-Ras(N17)		
$D_1(\mu m^2/s)$	1.02 ± 0.02	0.94 ± 0.01
$D_2(\mu m^2/s)$	0.16 ± 0.03	0.10 ± 0.01
α	0.84 ± 0.05	0.86 ± 0.01
H-Ras(V12)		
$D_1(\mu m^2/s)$	0.85 ± 0.04	0.73 ± 0.01
$D_2(\mu m^2/s)$	0.16 ± 0.04	0.10 ± 0.01
$L(nm)$	217 ± 46	179 ± 10
α	0.61 ± 0.05	0.63 ± 0.01

describes the positional error in one dimension. Either the positional accuracy has to be determined independently or the time-lag Δt must be varied so that the real diffusion coefficient can be obtained from the slope of Eq. 16. Note that this problem does not interfere with the method presented here; e.g., in the case of normal diffusion of one or two molecular species, the functional form of the cumulative probability distribution P_{cum} remains unchanged. For other diffusion modes, the correct form of P_{cum}, which might be altered due the finite positional accuracy, has to be employed. An extensive discussion can be found in Martin et al. (28).

Finite exposure/frame integration time

The fact that the fluorescence signal collection and integration time is finite can lead to erroneous results, in particular for confined diffusion (29,30). However, it was shown in Destainville and Salome (30) that the true values for the diffusion coefficient and the size of the confinement area can be retrieved from the data anyway. For the analysis performed above we assume that the influence of confinement or a finite exposure time on the cumulative probability distribution $P_{cum}(l, \Delta t)$ is negligible compared to the experimental error. This is quantified by the criterion given in Destainville and Salome (30): if L is the linear size of the confinement, D is the diffusion coefficient, and T is the exposure/integration time, then $T \ll L^2/12D$ should be fulfilled. This is indeed the case for the experiments presented above with $L \approx 0.18 \ \mu m$, $D = 0.1 \ \mu m^2/s$, and $T = 3$ ms. So, it is sensible to expect a distribution representing normal diffusion. It should, however, be stressed that our method works in principle for arbitrary forms of $P_{cum}(l, \Delta t)$.

Bleaching and blinking

Because of blinking and bleaching, single-particle trajectories of biologically relevant fluorophores inside cells are usually short ($\approx$10 steps). Given that p_{off} is the probability per time-lag Δt that a molecule turns dark or is not found by the peak-fitting algorithm (see also Appendix B), only a fraction $(1 - p_{off})$ of all diffusion steps is observed. Under the assumption that bleaching is independent of the size of a diffusion step, P_{cum} is reduced by a factor $(1 - p_{off})$. One consequence is that the figure of merit (Eq. 9) must be generalized to

$$\eta = \frac{1}{(1-p_{off})}\sqrt{16\pi ln2\frac{cD\Delta t}{M}}. \quad (17)$$

Accordingly Eq. 10 changes to

$$8\pi \ ln2\frac{cD\Delta t}{(1-p_{off})} \ll 1. \quad (18)$$

The second consequence is that the experimental correlation function C_{cum} has to be normalized to 1, after subtraction of the correction term $c\pi l^2$, to yield P_{cum} (see also Appendix B). Correspondingly, the theoretical distribution function has to be divided by $P_{cum}(l_{max}, \Delta t)$ where l_{max} is the maximal l included in the analysis.

APPENDIX B: CORRECTION FOR POSITIONAL CORRELATIONS DUE TO DIFFRACTION

Due to diffraction, the imaged Airy disks of the fluorescent molecules have a finite width and two molecules separated by a distance smaller than this width cannot be resolved. Therefore, one or both molecules will be absent in the position data. Consequently, fewer molecules are found close to each other than expected from the average molecule density. Thus, the molecule positions that ultimately enter into the analysis are effectively correlated. In the cumulative correlation function C_{cum}, determined from experimental data, this is visible as a dip for small step-sizes, see Fig. 8.
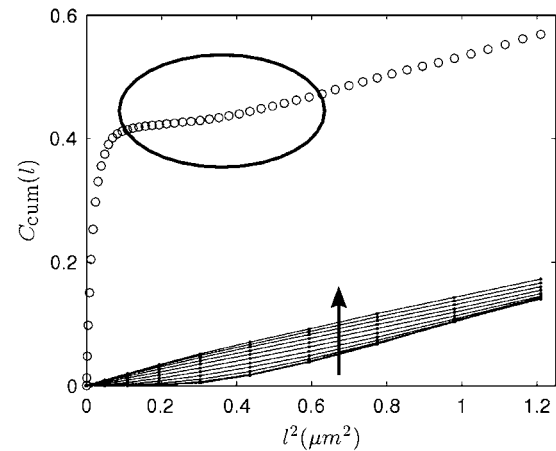
FIGURE 8 Correction for random spatial proximity of molecules at short distances and short time lag. The dip in the data obtained for individual H-Ras(N17) molecules at the apical side of 3T3-A14 cells taken at a time delay of 5 ms is due to diffraction (*open circles*, raw data; *solid lines*, pure spatial correlation for distances r from an arbitrary molecule; and $r = 0 \ \mu m$, 0.11 μm, 0.22 μm, ..., 1.21 μm where r rises in the direction of the *arrow*).

Since the correlation length is of the order of the peak width ($\approx$0.4 μm) this effect is only observable for small step-sizes, i.e., for slowly diffusing molecules or small time lags. To circumvent this problem, we adapted our algorithm in the following way: in the simple estimation, the number of ''wrong'' connections that the algorithm makes is described by the quadratic correction term $c\pi l^2$; now the amount of molecules that are found within a certain radius depends on the size of the diffusive step. If the molecule turns dark during the time lag there is no correlation. Therefore Eq. 5 is generalized to

$$C_{cum}(l, \Delta t) = (1 - p_{off})P_{cum}(l, \Delta t) + p_{dark}c\pi l^2$$
$$+ (1 - p_{dark})\int_0^\infty dr \ s(r,l)\frac{\partial P_{cum}}{\partial r}(r, \Delta t), \quad (19)$$

where the function $s(r, l)$ gives the number of molecules in a circle with radius l if the diffusive step-size is r. The expression $\partial P_{cum}(r, \Delta t)/\partial r$ gives the probability for a step of length r. The value p_{dark}—the probability per time-lag that a molecule turns dark—is estimated once and kept fixed for all data sets. For the data analyzed above, $p_{dark} = 0.3$ was used. The value p_{off} is the probability that a molecule either turns dark or is not found by the molecule-fitting routine, e.g., since it came too close to another molecule. The value $1 - p_{off}$ can be estimated by the height of C_{cum} after subtraction of the correction term. The value $s(r, l)$ is determined empirically from the experimental data by application of the algorithm defined in the beginning where, however, images I_a and I_b are identical. Furthermore, the center of the circle, with radius l, in which the molecules are counted, is translated by a vector of length r in arbitrary direction. The average over 20 equally spaced directions results in the array of curves depicted in Fig. 8. Subsequent to the calculation of $s(r, l)$ the correction is determined numerically by the following self-consistent algorithm:

Step 1. As an initial guess for the correction term, determine the slope of the linear part of C_{cum} and use the original correction term from Eq. 5.
Step 2. Subtract the correction.
Step 3. Normalize to 1 and fit the model.
Step 4. Calculate the new correction according to Eq. 19; go back to Step 2.

Steps 2–4 are repeated until the fit parameters change less than a predefined threshold. Note that this approach to correct for the effective correlation of

the peak positions only works because the effect is the same for all molecules. If positional correlations that are different for different molecules become important, the approach is no longer functional.

REFERENCES

1. Geerts, H., M. de Brabanter, R. Nuydens, S. Geuens, M. Moeremans, J. de Mey, and P. Hollenbeck. 1987. Nanovid tracking: a new automatic method for the study of mobility in living cells based on colloidal gold and video microscopy. *Biophys. J.* 52:775–782.

2. Eigen, M., and R. Rigler. 1994. Sorting single molecules: application to diagnostics and evolutionary biotechnology. *Proc. Natl. Acad. Sci. USA.* 91:5740–5747.

3. Ghosh, R., and W. Webb. 1994. Automated detection and tracking of individual and clustered cell surface low density lipoprotein receptor molecules. *Biophys. J.* 66:1301–1318.

4. Jacobson, K., E. D. Sheets, and R. Simson. 1995. Revisiting the fluid mosaic model of membranes. *Science.* 268:1441–1442.

5. Petersen, N., P. Hoddelius, P. Wiseman, O. Seger, and K. Magnusson. 1993. Quantitation of membrane receptor distributions by image correlation spectroscopy: concept and application. *Biophys. J.* 165:1135–1146.

6. Costantino, S., J. W. D. Comeau, D. L. Kolin, and P. W. Wiseman. 2005. Accuracy and dynamic range of spatial image correlation and cross-correlation spectroscopy. *Biophys. J.* 89:1251–1260.

7. Singer, S. J., and G. L. Nicolson. 1972. The fluid mosaic model of the structure of cell membranes. *Science.* 175:720–731.

8. Simons, K., and D. Toomre. 2000. Lipid rafts and signal transduction. *Nat. Rev. Mol. Cell Biol.* 1:31–41.

9. Edidin, M. 2003. The state of lipid rafts: from model membranes to cells. *Annu. Rev. Biophys. Biomol. Struct.* 32:257–283.

10. Munro, S. 2003. Lipid rafts: elusive or illusive. *Cell.* 115:377–388.

11. Mukherjee, S., and F. R. Maxfield. 2004. Membrane domains. *Annu. Rev. Cell Dev. Biol.* 20:839–866.

12. Hancock, J. 2006. Lipid rafts: contentious only from simplistic standpoints. *Nat. Rev. Mol. Cell Biol.* 7:456–462.

13. Douglass, A. D., and R. D. Vale. 2005. Single-molecule microscopy reveals plasma membrane microdomains created by protein-protein networks that exclude OD trap signaling molecules in T cells. *Cell.* 121:937–950.

14. Nichols, B. 2005. Without a raft. *Nature.* 436:638–639.

15. Dahan, M., S. Levi, C. Luccardini, P. Rostaing, B. Riveau, and A. Triller. 2003. Diffusion dynamics of glycine receptors revealed by single-quantum dot tracking. *Science.* 302:442–445.

16. Michalet, X., F. Pinaud, L. Bentolila, J. Tsay, S. Doose, J. Li, G. Sundaresan, A. Wu, S. Gambhir, and S. Weiss. 2005. Quantum dots for live cells, in vivo imaging, and diagnostics. *Science.* 307:538–544.

17. Lommerse, P. H. M., B. E. Snaar-Jagalska, H. P. Spaink, and T. Schmidt. 2005. Single-molecule diffusion measurements of H-Ras at the plasma membrane of live cells reveal microdomain localization upon activation. *J. Cell Sci.* 118:1799–1809.

18. Schmidt, T., G. Schuetz, H. Gruber, and H. Schindler. 1995. Characterization of photophysics and mobility of single molecules in a fluid lipid membrane. *J. Phys. Chem.* 99:17662–17668.

19. Hebert, B., S. Costantino, and P. W. Wiseman. 2005. Spatiotemporal image correlation spectroscopy (STICS) theory, verification, and application to protein velocity mapping in living CHO cells. *Biophys. J.* 88:3601–3614.

20. Kolin, D. L., S. Costantino, and P. W. Wiseman. 2006. Sampling effects, noise, and photobleaching in temporal image correlation spectroscopy. *Biophys. J.* 90:628–639.

21. Saxton, M. J. 1997. Single-particle tracking: the distribution of diffusion coefficients. *Biophys. J.* 72:1744–1753.

22. Burgering, B., R. Medema, J. Maassen, M. van de Wetering, A. van der Eb, F. McCormick, and J. Bos. 1991. Insulin stimulation of gene expression mediated by p21Ras activation. *EMBO J.* 10:1103–1109.

23. Harms, G., L. Cognet, P. Lommerse, G. Blab, and T. Schmidt. 2001. Autofluorescent proteins in single-molecule research: applications to live cell imaging microscopy. *Biophys. J.* 80:2396–2408.

24. Kusumi, A., Y. Sako, and M. Yamamoto. 1993. Confined lateral diffusion of membrane receptors as studied by single particle tracking: effects of calcium-induced differentiation in cultured epithelial cells. *Biophys. J.* 65:2021–2040.

25. Murakoshi, H., R. Iino, T. K. T. Fujiwara, C. Ohshima, A. Yoshimura, and A. Kusumi. 2004. Single-molecule imaging analysis of Ras activation in living cells. *Proc. Natl. Acad. Sci. USA.* 101:7317–7322.

26. Niv, H., O. Gutman, Y. Kloog, and Y. Henis. 2002. Activated K-Ras and H-Ras display different interactions with saturable nonraft sites at the surface of live cells. *J. Cell Biol.* 157:865–872.

27. Rotblat, B., I. Prior, C. Muncke, R. Parton, Y. Kloog, Y. Henis, and J. Hancock. 2004. Three separable domains regulate GTP-dependent association of H-Ras with the plasma membrane. *Mol. Cell. Biol.* 24:6799–6810.

28. Martin, D. S., M. B. Forstner, and J. A. Kaes. 2002. Apparent subdiffusion inherent to single particle tracking. *Biophys. J.* 83:2109–2117.

29. Ritchie, K., X.-Y. Shan, J. Kondo, K. Iwasawa, T. Fujiwara, and A. Kusumi. 2005. Detection of non-Brownian diffusion in the cell membrane in single molecule tracking. *Biophys. J.* 88:2266–2277.

30. Destainville, N., and L. Salome. 2006. Quantification and correction of systematic errors due to detector time-averaging in single-molecule tracking experiments. *Biophys. J.* 90:L17–L19.